Ceramics International 49 (2023) 33275–33290

Contents lists available at ScienceDirect

Ceramics International

journal homepage: www.elsevier.com/locate/ceramint

On the benefits of vegetable oil addition for the pore structure and acid resistance of alkali-activated systems

O. Rudić [a,*], F. Mittermayr [a], G.J.G. Gluth [b], S. Simon [b], N. Ukrainczyk [c], Y. Seyrek [a], B. Freytag [d], J. Juhart [a], C. Grengg [e]

[a] Institute of Technology and Testing of Building Materials, Graz University of Technology, Inffeldgasse 24, 8010, Graz, Austria
[b] Division 7.4 Technology of Construction Materials, Bundesanstalt für Materialforschung und -prüfung (BAM), Unter den Eichen 87, 12205, Berlin, Germany
[c] Institute of Construction and Building Materials, TU Darmstadt, Franziska-Braun-Straße 3, 64287, Darmstadt, Germany
[d] Laboratory for Structural Engineering, Graz University of Technology, Inffeldgasse 24, 8010, Graz, Austria
[e] Institute of Applied Geosciences, Graz University of Technology, Rechbauerstraße 12, 8010, Graz, Austria

ARTICLE INFO

Handling Editor: Dr P. Vincenzini

Keywords:
Alkali activated composites
Vegetable oil
Soap phase
Microstructure
Acid resistance and durability

ABSTRACT

The impact of high additions of vegetable oil (12 vol%) on the mechanical and microstructural properties of metakaolin-slag-based alkali-activated materials (AAMs) was studied. The addition of oil resulted in a slight decrease in initial polymerization kinetics but did not affect the final degree of reaction. AAM-oil-composite-mortars exhibited approximately ~30% lower compressive strength primarily due to the entrainment of air voids. Newly formed soap phases significantly reduced the volume of small capillary and gel pores (pore radii <15 nm), leading to a decrease in specific inner surface area by a factor of up to 15. The porosity modification induced by the oil addition greatly enhanced the resistance of AAMs against sulfuric acid attack, shifting the dominant processes from diffusion and cracks to framework-dissolution controlled by the inherent phase stabilities. Following the immersion in sulfuric acid ($pH_{stat} = 2$) for 8 weeks, the depth of corroded layer decreased by 70% and no cracks due to expansive phases were observed. These promising findings suggest that the incorporation of vegetable oil in AAMs has the potential to address durability concerns associated with diffusion-based corrosion processes, thereby expanding the range of future applications.

1. Introduction

In the last couple of decades, the application range of alkali-activated materials (AAM) [1], often also referred to as geopolymer materials (GPM) [2], as an alternative to Portland cement-based binder systems is increasing [3,4]. Despite significant research effort and developments achieved so far, several durability related aspects of AAMs still present unsolved issues which need to be better understood to enable broader applications [5–7]. Among those are reaction/diffusion-based degradation processes, such as carbonation, chloride penetration, acid - and sulphate attack, as well as water vapour diffusion processes resulting in autogenous and drying shrinkage [8–11]. The impact of all of the above-mentioned degradation processes on AAM performance are directly influenced by the pore structure [12]. Accordingly, methods and concepts to optimize the microstructure bear high potential to increase the overall performance of AAMs and build the basis for broader applications.

The addition of vegetable (waste) oil as an eco-friendly additive to modify concrete microstructural properties has been explored for Portland cement-based systems [13–16]. However, the incorporation of organic oils, fats or their respective fatty acids into Portland Cement (PC) leads to a significant retardation of the hydration reactions. Reasons therefore are that organic liquids may act as ligands but usually do not form strong chemical bonds within the PC microstructure [17,18]. Abousnina et al. [19] showed that an oil content higher than 2 wt% suppressed the C_3S and C_3A hydration and increased the pore sizes due to the higher amount of free water which remains unused during the hydration process. Beside increased porosity, the addition of fatty acids reduced the strength development due to calcium incorporation into metal-soaps, rather than in C–S–H, which may further lead to a lower total amount of hydration products.

To date, oil addition in AAMs were mainly studied in the context of mineral oils, e.g. radioactive wastes encapsulation [20,21], or the production of highly porous AAM composites and foams, exhibiting high

* Corresponding author.
E-mail address: ognjen.rudic@tugraz.at (O. Rudić).

https://doi.org/10.1016/j.ceramint.2023.08.036
Received 17 May 2023; Received in revised form 22 July 2023; Accepted 2 August 2023
Available online 3 August 2023

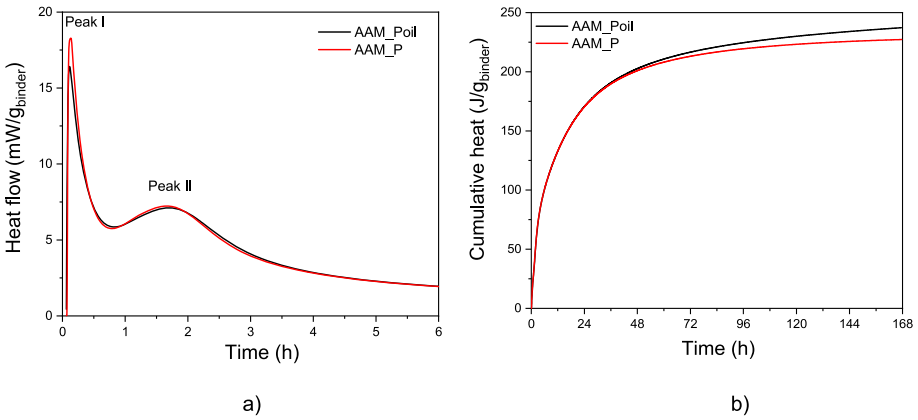

Fig. 1. Isothermal calorimetric response of AAM_P and AAM_Poil pastes at 20 °C a) normalized heat flow, and b) normalized cumulative heat.

specific surface area and high ion exchange capacity/efficiency [22–25]. Therein, hydro-soluble soap molecules (surfactants) and glycerol were formed due to an ongoing saponification reaction. Formed soap and glycerol phases were then removed by immersion in warm water or thermal treatment [26] to enable development of the high porosity. Likewise, AAM foams with high porosity were studied using vegetable oils as low-cost stabilizing agents and hydrogen peroxide (H_2O_2) solution as pore forming agent [27]. To date, no efforts were made to examine the possibility of using saponification of vegetable (waste) oil in the alkaline environment during alkali activation to increase material durability and performance. Lambertin et al. [28,29] investigated preferential water flow pathways and water permeability of hardened AAM-oil composite mortars. However, these authors used mineral oils that do not form soaps. To the best knowledge of the authors, only Huang et al. [30] studied the impact of vegetable oil with respect to the autogenous shrinkage behaviour of AAM concrete.

This paper focuses on the changes in physicochemical material properties due to the addition of vegetable oil as a permanent porosity modifier within metakaolin-slag-based AAMs. The main aim was to modify the pore structure in a way to reduce diffusion related processes and to increase the material performance for future applications in (bio) chemically aggressive environments, such are sewer systems [31]. The impact of oil addition on the polycondensation kinetics, the phase assemblages of the inorganic gel phase, the pore structure, as well as the phases formed due to saponification reactions, was characterized using various porosity measurements (Mercury intrusion porosimetry - MIP, Nitrogen adsorption - NAD), together with advanced spectroscopic (Raman-imaging, infra-red spectroscopy - FT-IR) and microscopic (environmental scanning electron microscopy - ESEM, electron probe microanalyses-EPMA) analytics. In order to investigate potential durability enhancements in respect to acidic environments, material response in sulfuric acid ($pH_{stat} = 2$, for 8 weeks) with and without oil addition was recorded.

2. Materials and methods

2.1. Raw materials

Alkali activated paste (AAM_P) and mortar (AAM_M) samples were produced by mixing a Fe-rich metakaolin/ground granulated blast furnace (MK-GGBFS) powder described in details by Juhart et al. [32]

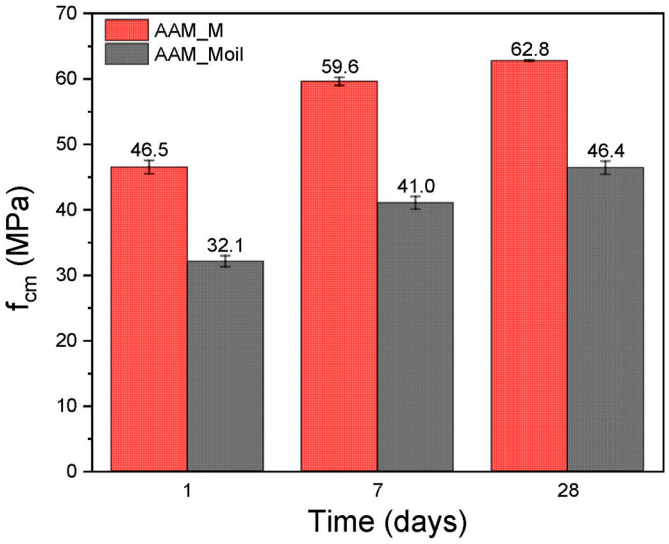

Fig. 2. Compressive strength (f_{cm}) development of AAM_M and AAM_Moil with time.

(AAM_powder) with a potassium-based alkali activator (waterglass, WG, with a solid content of 56.6 wt% and a SiO_2/K_2O molar ratio of 1.92, according to manufacturer information) and water. The materials used were industrial products and were previously available as "banahCEM" [33]. A heat treated (175 °C) commercial sunflower oil (density 0.92 kg/m^3) was used as the organic modifier for both paste (AAM_Poil) and mortar (AAM_Moil) samples. For mortar samples, siliceous sand was added as aggregate, exhibiting a grading between 0.08 and 4 mm (Fig. A.1, Appendix). The chemical compositions of both AAM_powder and the WG, obtained by means of X-ray fluorescence (XRF) analysis, are presented in Table 1.

The mineralogical composition of the AAM_powder (Fig. A.2, Appendix), obtained by means of X-ray diffraction (XRD), reveals hematite (Fe_2O_3) as the dominant crystalline mineral phase, followed by noticeable lower amounts of meta-halloysite [$Al_2Si_2O_5(OH)_4$] [34,35], anatase (TiO_2) and quartz (SiO_2). The prominent hump in the diffractogram in the range 20–45° of 2θ is attributed to the presence of an amorphous

Table 1
Chemical composition of the AAM_powder and WG in wt.%.

Raw materials	SiO_2	Al_2O_3	K_2O	CaO	Fe_2O_3	MgO	Na_2O	TiO_2	SO_3	H_2O
AAM_powder	33.90	24.80	0.23	14.00	18.20	3.47	0.24	2.33	0.95	
WG	30.25		26.34							43.41

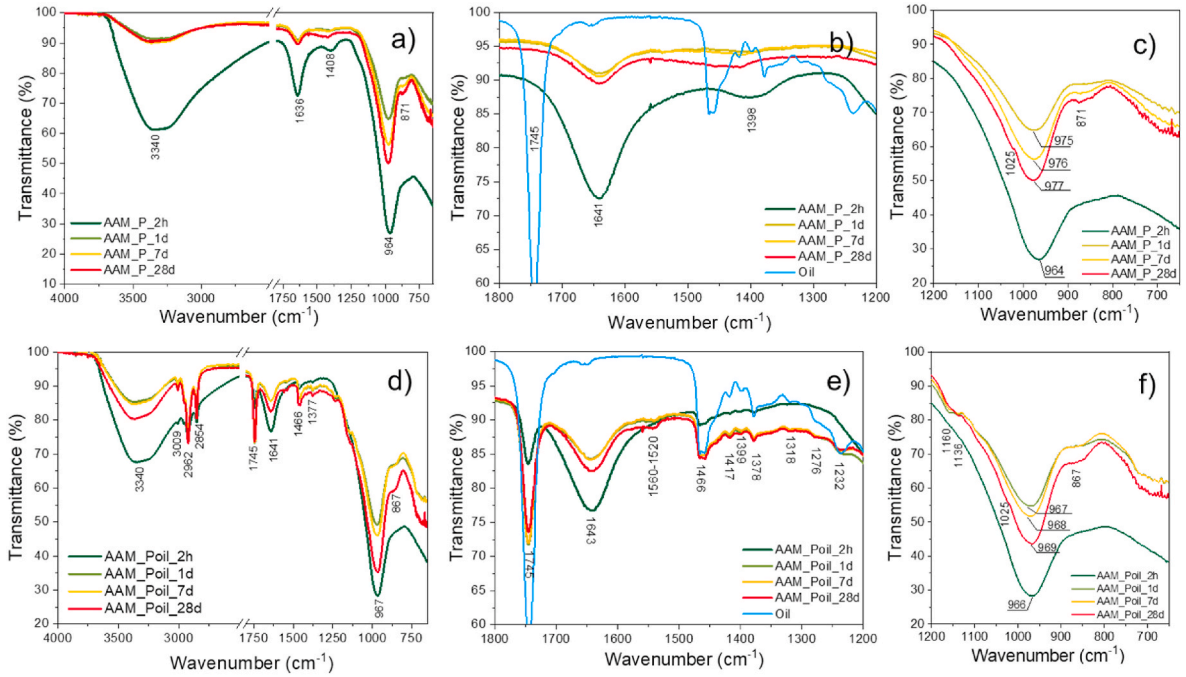

Fig. 3. ATR-FTIR spectra of AAM_P and AAM_Poil up to 28 days of hardening within the various wavenumber values ranges.

phase as the major constituent of the material.

ATR-FTIR analysis of the AAM_powder showed the absence of narrow stretching and bending vibration bands of hydroxyl (OH) molecular groups, usually observed around 3400 cm^{-1} and 1660 cm^{-1}, respectively (Fig. A.3, Appendix). Nevertheless, weak, broad bands are observed in these wavelength regions, indicating the presence of minor amounts of residual water in the material. The main absorption peak at 1030 cm^{-1} is assigned to Si–O–Si(Al) vibrations of Q^3 sites in the meta-halloysite and the amorphous phase. The broad peak in the range of 900-750 cm^{-1}, centred at approximately 830 cm^{-1} is probably linked to stretching vibration of Si–O–Si(Al) of different Al-coordination with a low degree of polymerization [36,37].

The evaluation of the molecular functional groups and vibration modes of the vegetable sunflower oil was performed by ATR-FTIR. The spectra (Fig. A.3, Appendix) show linoleic and linoleic acyl groups [38, 39], as the main constituents of the sunflower oils.

2.2. Sample preparation and mixing protocol

The AAM pastes were produced by mixing the AAM_powder, WG, water, following the procedure described in detail by Juhart et al. [32]. Volumes of approx. 1.2 L were prepared using a 4.5 l (total volume) planetary lab-mixer according to EN 196-1 [40]. To avoid large inhomogeneous oil droplet size distribution, a short pre-emulsification process was applied, as the sunflower oil was added to the activator/water mix and stirred for 30 s at 150 rpm. Then, the solid precursor was added to the water-activator-oil emulsion and mixed for 150 s at 150 rpm, followed by mixing with 300 rpm for another 30 s. Finally, fresh mortar mixes were prepared by mixing the obtained paste slurry with quartz sand (density of 2620 kg/m^3) with a maximum grain size of 4 mm for another 150 + 30 s at 150 rpm and 300 rpm, respectively. Paste and mortar mixes were poured in plastic moulds (prisms of 40x40 × 160 mm for mortar; cylindrical 40 × 40 mm for pastes) and compacted using a vibration table for 1 min. Poured fresh pastes and mortars were covered and stored at >95% relative humidity (RH) and 20 °C for 24 h. Thereafter, they were demoulded and continuously cured at >95% of RH and at 20 °C until the respective tests were performed. Complete mixing proportions of investigated paste and mortar mixes, together with the air content and density are given in Table 2.

2.3. Physicochemical and microstructural characterization of pastes and mortars

2.3.1. Isothermal calorimetry and compressive strength

Test specimens for isothermal calorimetry (I-Cal 4000 HPC) were produced as follows: paste mixes (50 g of AAM_powder, 34.7 g of WG, 15.6 g of water and in case of AAM_Poil 15.6 g of oil) were mixed with a Vortex-mixer (Velp Scientifica ZX4) at 2400 rpm in a standard calorimetry container (~120 ml) for 120 s and immediately transferred to an isothermal calorimeter (I-Cal 4000 HPC). Specific heat flow and cumulative heat were calculated in relation to mass of binder (AAM_powder + solid part of WG). The heat release was measured at 20 °C for 7 days, with 6 acquisitions per minute during the first 30 min and 1 acquisition per minute afterwards until the end of measurement.

The compressive strength of mortar samples was tested in accordance with EN 196-1 [40] on 160 x 40 × 40 mm prisms after 1, 7 and 28 days. Every specimen was prepared as triplicate and an average value was taken during each test.

Table 2
Composition of paste and mortar samples per kg/m^3. Air content and density analyses conducted according to Ref. [41]; n.m.: not measured.

ID	AAM_powder (kg/m^3)	WG (kg/m^3)	Water (kg/m^3)	Oil (kg/m^3)	Sand 0/4 (kg/m^3)	Air content (vol%)	Density (kg/m^3)
AAM_P	392	272	122	0	0	n.m.	n.m.
AAM_Poil	392	272	122	122	0	n.m.	n.m.
AAM_M	392	272	122	0	1520	2.8	2193
AAM_Moil	392	272	122	122	1520	3.7	2027

2.3.2. Microstructural characterization methods

The mineralogical composition of the AAM_powder and the paste samples were characterized by X-ray diffraction (XRD) using a PANalytical X'Pert PRO diffractometer equipped with a Co-radiation source (40 kV, 40 mA), 0.5° antiscattering and divergence slits and a Scientific X'Celerator detector. The tests were carried out from 5 to 80° of the 2θ range with a step size of 0.008°. Mineral identification was determined with the PANalytical X'Pert HighScore software (version 2.2e) and a pdf-4 database.

Fourier-transform infrared spectroscopy (FTIR) was performed on a PerkinElmer Frontier spectrometer using the attenuated total reflectance (ATR) configuration. Mid-infrared (MIR) spectra were obtained in the range from 650 to 4000 cm^{-1} at a spatial resolution of 2 cm^{-1}. The MIR spectra were processed using background subtraction and ATR correction algorithms of the Spectrum 10 software suite. Paste samples after 2 h, 1, 7 and 28 days were analysed. The relative absorbance spectra over the range of 1200–900 cm^{-1} were subjected to a deconvolution analysis employed by a peak deconvolution tool (from Origin 2019) with Gaussian peak shapes and variable peak widths. Deconvoluted FTIR spectra were used to display the structural modification, phase assemblages and the chemical arrangements [42,43].

Raman spectroscopy of freshly fractured surfaces of paste samples was obtained using a confocal Alpha300R instrument (WITec, Germany) with an excitation wavelength of 532 nm and a power of 4 mW at room temperature. The spectrometer grating had 600 lines/mm, yielding a resolution of ~4.5 cm^{-1}. A lens with a magnification of 100x was used, resulting in a diameter of the incident focused laser beam of ~1 μm. For AAM_Poil, Raman maps were acquired by moving the sample stage in 0.65 μm increments in the x- and y-direction along the surface of the sample to acquire spectra in the area of interest with an accumulation time of 0.7 s per spectrum. Additional spectra of selected locations were acquired for AAM_P and AAM_Poil with 5 s accumulation time (30 repeated acquisitions to increase signal-to-noise ratio). Measurements were performed in the region 50–4000 cm^{-1}. Background correction and normalization of the spectra were carried out with the Witec software Project Four 80/160. False-colour Raman maps were constructed with the same software by assigning a colour (blue, red, and green, respectively) to regions of the scans with their main spectral features at 2910, 1355 and 151 cm^{-1}, respectively, based on an analysis of the different spectra of the scanned area.

The chemical composition of the mortar samples was additionally determined by thermogravimetric (TG) analysis performed on a NETZSCH STA 409 EP, with 80 mg of each sample powder being heated from 30 °C to 1000 °C at a constant heating rate of 10 °C/min under air atmosphere. Air flow, instead of N_2 flow, was used in order to enable the sunflower vegetable oil to fully decompose.

2.3.3. Pore structure characterization methods

The pore structure of hardened AAM mortars was investigated by mercury intrusion porosimetry (MIP), nitrogen adsorption (NAD) and dynamic vapour sorption (DVS) methods.

MIP data were obtained using a Pascal 440 Thermo-Scientific device. Mercury (density 13.53 g/cm^3, surface tension 0.485 N/m and contact angle 130°) was used for calculating the pore size distribution (PSD) by applying the Washburn equation [44]. Tested samples were gently chopped, and approximately 1g of total weight was used for analysis. The MIP measurements were applied to characterize the pore size ranges from 3 nm (due to the maximal possible applied pressure of 440 MPa) to approximately 80 μm. However, the high pressure necessary to enable mercury penetration might alter the fragile microstructure [45], especially in the ranges of smaller size pores.

NAD isotherm analyses were carried out on hardened mortar specimens at 77K (i.e. -196.15 °C) temperature using a BELSORP-mini X (Microtrac MRB, Pennsylvania, USA). For the measurements, specimens were gently chopped, sieved (1 mm sieve) and approximately 1 g of their total weight was used for analysis and vacuumed (down to 10 Pa overnight) to remove moisture. NAD method was used to characterize pore ranges up to 50 nm of pore radii (R_p) size.

The DVS analyses were conducted using a Dynamic Water Vapour Sorption Analyzer (GraviSorp 120; Porotec) device. This test provides information regarding the gel pore (up to 50 nm sizes of R_p) structure, measuring the equilibrium between the water content of the sample and the relative humidity at a constant temperature [46–48]. Test pieces (approximately 2 g of bulk/solid sample) were placed on a dish within the DVS chamber, without any pre-treatment, such as drying by vacuum or temperature treatment [49]. Adsorption and desorption isotherms were recorded between 5 and 94% of RH at 25 °C. The levels of RH were obtained by mixing proportional amounts of dry and humid air 1 m/s of an air speed.

Based on the NAD and DVS adsorption data, the Barrett–Joyner–Halenda (BJH) model was used to derive PSD curves of the desorption isotherm branches [50]. By using the Brunauer–Emmett–Teller (BET) model, the specific surface area (S_p) of investigated materials was evaluated [51]. Five pore size radii ranges were distinguished in accordance to Zhu et al. [52]: (i) gel pores 1–5 nm, (ii) fine capillary pores 5–25 nm, (iii) middle capillary pores 25–50 nm, (iv) large capillary pores 50–5000 nm and (v) macro pores >5000 nm.

The presence, shape and size of air voids of the investigated paste and mortar samples were determined on cross-sections (40 × 40 mm) at an age of 28 days. The cross-sections were analysed with a light microscope (Keyence VHX 5000 3D-microscope; 20-200 x magnification) under normal light. Additionally, polished paste samples were analysed using a scanning electron microscopy in the environmental mode (ESEM, Zeiss EVO LS25), equipped with back scattered (BSE), secondary electrons (SE) and energy dispersive spectrometer (EDS) detectors (EDAX, AMETEK, Berwyn, USA). Operating conditions in the environmental SEM were kept at low vacuum mode at 10 Pa to prevent charging effects on the samples, while eliminating the use of conductive coatings.

2.3.4. Durability in relation to acid resistance

Acid exposure tests on mortars were carried out on 40 x 40 × 40 mm samples using an automatic titration reactor set-up, presented previously by Grengg et al. [31]. Each mortar specimen was placed into an individual reaction vessel (volume 1000 ml) over a floating magnetic stir bar rotating at 150 rpm and was submerged in 720 ml diluted sulfuric acid (96% Suprapur, Sigma-Aldrich) solution exhibiting a pH of 2. During the exposure period of 8 weeks, the pH of the solution was kept constant at pH = 2 by titration of a 3 M sulfuric acid solution using a peristaltic pump. The amount of acid dosage and pH value was permanently recorded using a computer controlled titrator device (Schott; TitroLine alpha plus). Specific electric conductivity (EC) was externally measured using a WTW Multi350i instrument, equipped with a TetraCon325 electrode during liquid sampling periods. Liquid samples were extracted after 10 min; after 1, 2, 4, 8, 16 h; after 1, 2, 4 days; and after 1, 2, 3, 4, 5, 8 weeks. At each sampling, 3 ml of experimental solution was extracted with a syringe, filtered through a 0.45 μm cellulose acetate membrane and diluted with MilliQ water (Ω = 18.2 μs/cm). Subsequently, major, minor and trace elemental concentrations were analysed via inductively coupled plasma – optical emission spectrometry (ICP-OES; analytical error: <5%), using a PerkinElmer Optima8300DV inductively coupled plasma optical emission spectrometer. The dissolved organic carbon (DOC, in mg/l) was analysed on 40 x 40 × 40 mm cube specimens using a Shimadzu DOC-VcPH + ASI-V Analyzer, with an analytical error below 5%.

After the acid exposure, mortar samples were dried for 48 h at 40 °C. Thereafter, they were embedded in epoxy resin under vacuum conditions in order to guarantee the abrasion-free continuative preparation of the deteriorated specimens. From the embedded samples, a cross section was cut, polished, carbon coated and analysed with an electron probe microanalyzer (EPMA) using a JEOL JXA8530F Plus Hyper Probe (JEOL, Tokyo, Japan), equipped with a field-emission gun (FEG). (Semi)-quantitative element distribution images of Al, Ca, K, Si and S were

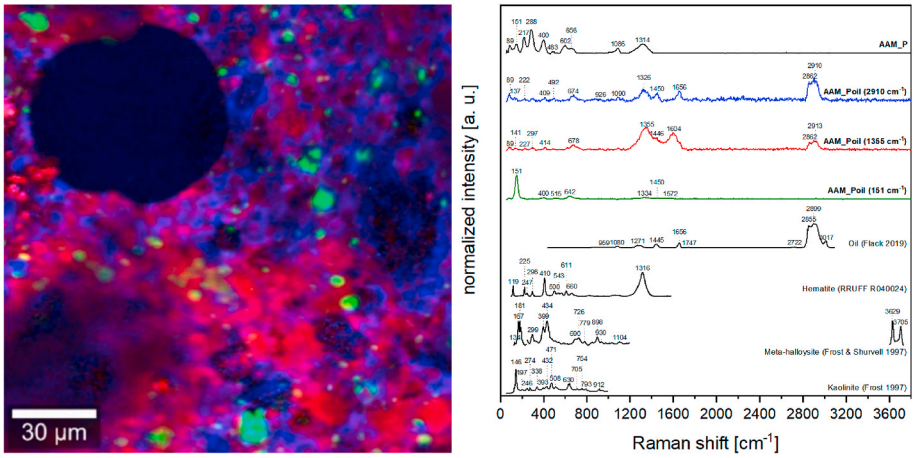

Fig. 4. a) False-colour Raman map of AAM_Moil. Coloured regions are characterized by main peaks: blue at 2910 cm^{-1} (representing a high oil fraction), red at 1355 cm^{-1}, and green at 151 cm^{-1}. The dark, circular feature in the top left corner is an air void. (b) Raman spectra corresponding to the blue, red and green regions in the Raman map, together with Raman spectra of a reference AAM_M sample, olive oil, hematite, meta-halloysite and kaolinite. (For interpretation of the references to colour in this figure legend, the reader is referred to the Web version of this article.)

recorded in a way to represent the corroded layers, the transition zone and the intact matrix. The quantification of the individual element mappings in wt.% were performed against mineral standards (microcline for Al, K and Si; augite for Ca; illmenite for Fe; baryte for S). Elemental mappings were recorded at 15 kV and 30 nA, with a dwell time of 15 ms and a step size of 5 µm.

3. Results and discussion

3.1. Effects of oil addition on the reaction kinetics and compressive strength development

The influence of oil addition on the reaction kinetics of AAM_P and AAM_Poil samples up to 7 days of hardening was characterized by isothermal calorimetry. The calorimetric curves (Fig. 1) of AAM_P and AAM_Poil mixtures show two main peaks, where each peak corresponds to heat release due to distinct processes during alkali activation [53,54]. The first narrower peak (Peak I) of initial heat release corresponds to the particle wetting, dissolution of the AAM_powder particles and the initial formation of dissolved silicate units and their complexation with alkali ions [55,56]. The somewhat lower intensity of the Peak I in the case of AAM_Poil (Fig. 1a) may be attributed to a slightly lower dissolution degree of the AAM_powder in the presence of oil. As Peak I was observed at approximately the same time for both AAM_P and AAM_Poil, this effect may be attributed to physical rather than to specific chemical processes [57]. This peak is followed by a period of limited heat release, generally identified as the induction period, when reaction kinetics are reduced as a result of reduced reactive surfaces of unreacted AAM_-powder grains, or due to reaching a critical concentration of ionic species necessary to form further reaction products [57]. There are no visible differences in respect to the second peak (Peak II) between AAM_Poil and AAM_P (Fig. 1a). As Peak II is ascribed to the heat release during polymerization reaction and network formation [53,56,58], it can be deduced that differences regarding ongoing polymerization reaction and subsequent network formation upon the oil addition are negligible. This is in line with previously reported result in similar settings [59]. With extended time of reaction (i.e., after 24 h), a slightly higher heat release in the case of AAM_Poil can be observed (Fig. 1b), contributing to somewhat greater total heat release when oil is added. This may be ascribed to the development of additional microstructural features or slightly changed network reorganization due to the reaction between the oil component and the AAM paste in a highly alkaline environment.

The compressive strength (f_{cm}) of the AAM_Moil composite is reduced by 31%, 32% and 26%, after 1, 7 and 28 days of hardening, respectively, in comparison to AAM_M mortars (Fig. 2). Reason for the strong reduction of early strength values within the oil system could not be associated to reduced reaction kinetic due to oil addition, as shown by isothermal calorimetry (Fig. 1). Accordingly, the observed differences in f_{cm} *values* are more likely correlated to changes within the physical material properties, especially the increase in large singular air voids due to oil addition.

3.2. Effects of oil addition on mineralogical and chemical material properties

The detected crystalline phases after 28 days of curing did not display significant differences between AAM_P and AAM_Poil samples (Figure A2, Appendix). In order to acquire an integral view regarding chemical modifications of amorphous phase during the alkali-activation process, XRD was complemented with ATR-FTIR analyses after 2 h, 1, 7 and 28 days of curing (Fig. 3a and 3d).

Spectra within the wavenumber range between 1800 and 1200 cm^{-1} could be clearly linked to absorption peaks originating due to the presence of sunflower oil (Fig. 3e, Table A.1). With time, a decrease of the absorption peak at 1745 cm^{-1}, related to the presence of ester carbonyl functional groups of the triglycerides originating from oil, was observed (Fig. 3e). In addition to the noted oil peaks at 1466, 1417, 1399, 1377, 1236 and 1160 cm^{-1} (Fig. 3e, Table A.1), the spectra of AAM_Poil had a less prominent, yet visible broader peak in the wavenumber range of between 1520 and 1560 cm^{-1}, which was not observed in the reference material or the oil spectra. This peak might occur due to the existence of carboxylate asymmetric stretching vibrations, which are distinctive for the presence of metal soap phases based on the available cations (Ca, Fe, K, Al, Mg). This assumption is further supported by the observed decrease of the carbonyl group stretching vibration at 1745 cm^{-1}, followed by the appearance of two peaks, which are characteristic for the carboxylate group of fatty acids and metallic salts: 1) the asymmetric stretching vibration between 1600 and 1520 cm^{-1}, assigned to carboxylate ion of potassium benzoate (i.e. R-COO−M^{+}) [60,61] and 2) the symmetric stretching vibration between 1400 and 1430 cm^{-1} of carboxylate ion, partially overlapping with the initial adsorption peak of oil [62] (Fig. 3e).

In order to confirm saponification, pure oil and activator were mixed in accordance to the ratio given in Table 2 and their ATR-FTIR spectra after 5h and 3 months are presented in Figure A.3b, Appendix. Observed decrease and nearly disappearance of the absorption peak at 1745 cm^{-1} and, concurrent increase of the asymmetric and symmetric stretching vibrations of the carboxylate ion between 1540 and 1600 cm^{-1} and 1400 and 1430 cm^{-1} confirmed the development of the soap phases [63,

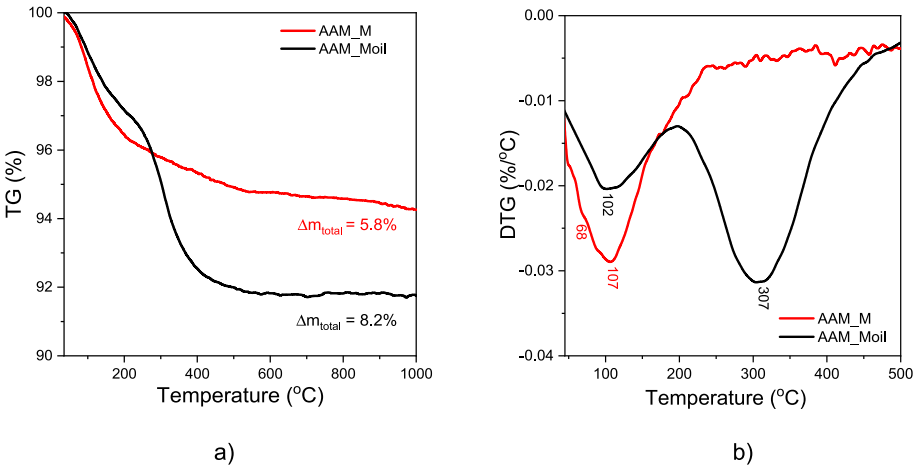

Fig. 5. Thermogravimetry analysis results of hardened mortars a) TG and b) DTG of AAM_M and AAM_Moil mortars.

64]. Additionally, a shift of the most intensive absorption peak from 966 cm^{-1}, originating from the activator, towards higher wavenumber values (may be seen at 966 and 977 cm^{-1}) with time. This shows that oil transforms towards a more soap-like organized structure due to saponification processes in this highly alkaline environment.

The broad band located between 900 and 1200 cm^{-1} (Fig. 3c and 3f) is associated with stretching vibrations of Si–O–Si(Al) [65–68]. Accordingly, the observed increase in intensities after the first day of hardening was associated with the growing share of amorphous aluminosilicate gel within the developed structure [69]. The shift of the Si–O–Si(Al) asymmetric stretching vibration from 1034 cm^{-1} in the case of the unreacted AAM_powder (Figure A.3, Appendix) towards lower wavenumbers of 964 cm^{-1} and 966 cm^{-1} for AAM_P and AAM_Poil (Fig. 3c and 3f), respectively, indicates the dissolution of original AAM_powder network upon the alkali activation and incorporation of other species (Al, K, Ca, etc.) within the newly formed polymerized network [70–72]. The newly formed, broad band can be fitted with three vibrations at ~1030, ~995, and 955–950 cm^{-1}, respectively (Figure A.4). While the first band is attributed to unreacted AAM_powder, the other two might be assigned to stretching vibrations of Si–O–Si(Al) in Q^4 sites in K-A-S-H gel with a high degree of Al-incorporation and stretching vibrations of Si–O–Si(Al) in Q^2 sites in C-(K-)A-S-H gel, respectively [67]. Namely, Yip and van Deventer [73] point out the co-existence of sodium/potassium aluminosilicate gel ((N,K)-A-S-H) and calcium silicate hydrate/calcium aluminosilicate gel (C–S–H/C-A-S-H) when metakaolin and slag blends are activated at a pH not high enough to precipitate all the reactive calcium. Additionally, in potassium silicate activated systems, formation of both C–S–H gel and potassium aluminosilicate hydrate (K-A-S-H) gel was observed [74]. In this regard, the developed gel phases could be characterized as the gel-like fine particles, which can be described as a K–(C)–A–S–H product, or mixed phase of K–A–S–H and C–A–S–H gels, as already shown in the literature [75–77]. Here, supported by literature, presence of C-(K-)A-S-H gel phase, or mix of C-A-S-H and K-A-S-H may be assumed, yet cannot be unambiguously confirmed.

In order to support conclusions drawn from ATR-FT-IR analyses and to get a better understanding of the oil distribution within the material, additional Raman spectroscopy images were recorded. Fig. 4a shows the Raman map of sample AAM_Moil; Fig. 4b displays the characteristic spectra for the colours shown in the map, a spectrum of sample AAM_M, and spectra of relevant reference minerals: hematite [78,79], meta-halloysite [80, 81], kaolinite [82]) as well as olive oil [83]. Olive oil is representative of the employed sunflower oil, as the Raman spectra of a number of vegetable oils, including sunflower oil and olive oil, differ only very slightly from each other [84].

The major difference between the spectrum of AAM_M and the spectra of AAM_Moil is the occurrence of peaks at 1450, 1656, 2862, 2910, and ~3010 cm^{-1} (weak) in the latter. These peaks can be clearly attributed to the sunflower oil in the composite (Fig. 4b). In detail, the peaks are assigned to CH bending of CH_2 (1450 cm^{-1}), C=C stretching (1656 cm^{-1}), CH stretching of CH_2 and CH_3 (2862 and 2910 cm^{-1}), and anti-symmetric = CH stretching (~3010 cm^{-1}) [83–85]. The peaks of the oil were particularly prominent in the blue regions in Fig. 5a, showing that it was not only contained in the air voids of the material; instead, the oil was finely dispersed on a length scale of a few microns. This contradicts the assumption that organic liquids in AAM_Moil composites are generally contained in larger voids [29], but are also well distributed in pores of smaller sizes.

The features at lower wavenumbers (<1400 cm^{-1}) in the spectra of AAM_M and AAM_Moil can be assigned to unreacted hematite, and meta-halloysite or kaolinite from the starting material (Fig. 5b). In addition, the peak observed in the spectra of AAM_M and AAM_Moil in the range 137–151 cm^{-1} is possibly also due to anatase, which exhibits Raman signals at ~145, 400, 516 and 640 cm^{-1} [78,86]. Quartz [78] likely contributed to the peaks at ~220 and ~490 cm^{-1}. No distinct peaks of the supposed reaction products C-(K-)A-S-H and K-A-S-H could be unequivocally discerned. This parallels an earlier Raman study on AAMs [86] and is likely due to the disordered structure of these phases, which can be expected to cause their peaks to be weak and broad and, thus, to be masked by the peaks of the other (crystalline) phases, which are more Raman-active. In addition to the peaks described above, the spectra of some regions of AAM_Moil contained a prominent peak with its maximum in the range ~1575–1605 cm^{-1} (Appendix Figure A.5); these regions were concentrated near the air void in Fig. 4. The assignment of the peak is currently uncertain, but it is possibly due to products of the reaction of the oil with the alkaline activator solution.

In order to understand the thermal stability of the soap phases formed, thermogravimetry (TG) and the corresponding differential thermogravimetry (DTG) of AAM_M and AAM_Moil composites after 28 days were performed (Fig. 5). The TG curves show a gradual weight loss of the investigated mortar samples (Fig. 5a), where the total weight losses of the AAM_M and AAM_Moil specimens are 5.8 and 8.2 wt% (Fig. 5), respectively. In particular, from the DTG curves (Fig. 5b), a high mass loss between 30 °C and 100 °C, observed for both samples, correlates to the release of free and loosely bound water [87]. The first weight loss peak at around 100–110 °C corresponds to the dehydration of gel phase [88]. The addition of oil causes a slight shift of the peak towards lower temperatures (from 107 °C to 102 °C) and reduces notably its intensity. This may be associated to the slightly modified incorporation of ion species (Ca, Al, K, etc) into the polymeric gel phase, altering its arrangement and favouring the formation of structurally modified amorphous structures [89]. The observed reduced weight loss

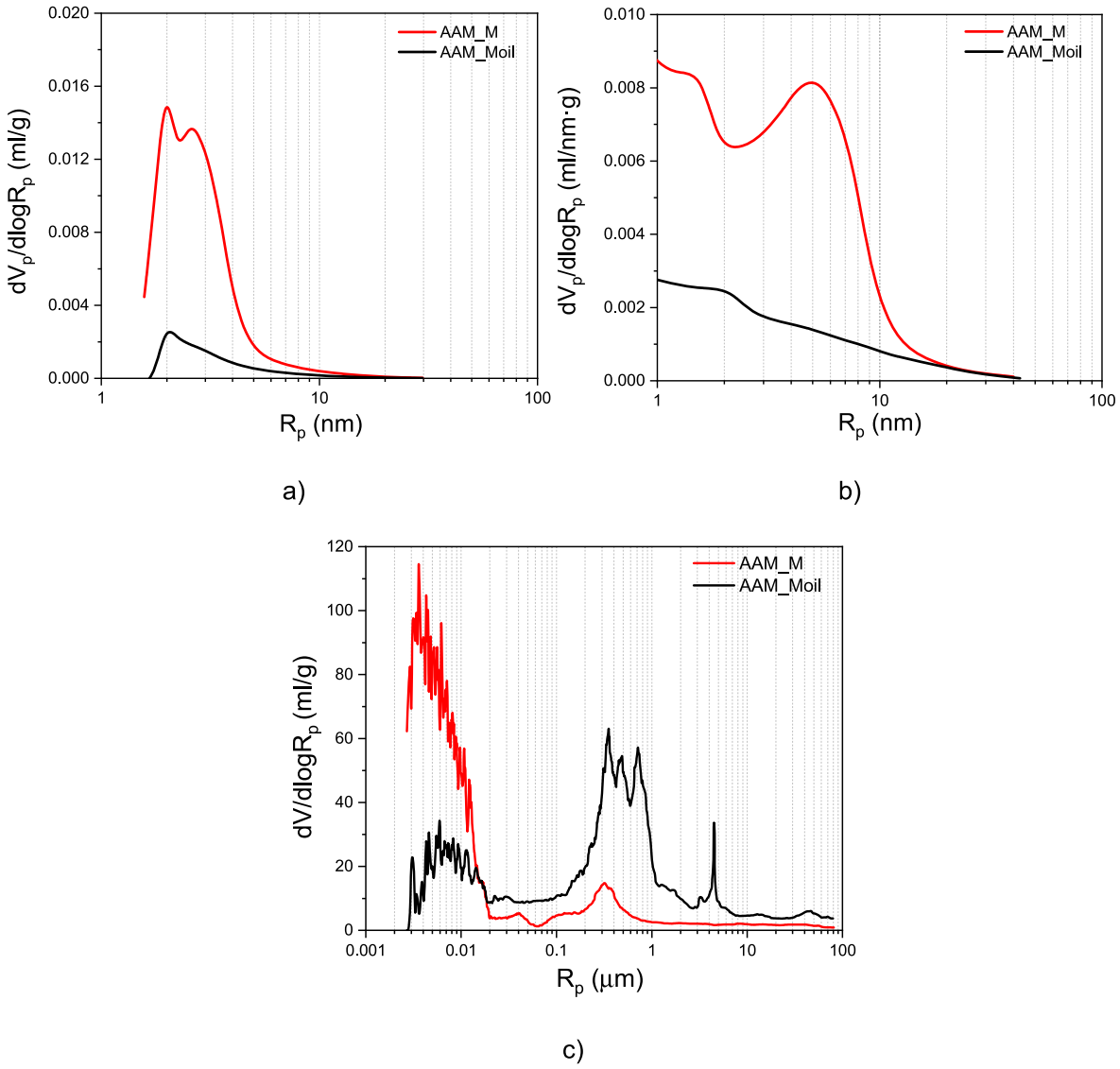

Fig. 6. PSD of AAM_M and AAM_Moil evaluated by a) NAD; b) DVS; c) MIP analyses.

within this temperature range measured for the AAM_Moil suggests overall lower water quantities within the polymeric gel phase with oil addition, The continuing weight loss between 100 °C and 180 °C corresponds to the further dehydration of C-(K)-A-S-H and K-A-S-H gel phases. The slightly lower mass loss and intensity of the corresponding peak up to 200 °C in case of the AAM_Moil sample may indicate an existence of lower volume of the developed gel phase. Beside described mass loss up to 200 °C, the main mass loss of the AAM_Moil composite occurs in the temperature range between 250 °C and 450 °C. This can be correlated to the decomposition of organic components (sunflower oil and developed soap phases) which usually takes place in three distinct stages: 1) degradation of saturated fatty acids, 2) degradation of unsaturated fatty acids and 3) oxidation of carbonaceous residue [90].

3.3. Effects of oil addition on pore structure

Results obtained from NAD and DVS exhibited strongly reduced specific surface area, i.e. S_p, from 46.72 m^2/g to 3.17 m^2/g and 77.14 m^2/g to 10.64 m^2/g, between the AAM_M and AAM_Moil composite, respectively, accounting for a reduction by a factor of up to 15. Thus, addition of oil significantly reduces the development of gel and small capillary porosity (Fig. 6), below 15 nm of pore R_p due to the saponification process. The variations in the absolute decrease in pore volume between the NAD and DVS analyses could be explained by higher penetration capacities of finer pores for smaller water molecules, compared to the larger nitrogen molecules [48].

The modification of the pore structure due to oil addition results in flattened PSD curves with no development of a dominant pore size, indicating a homogeneous reduction of the smaller pore fractions. The absence of dominant pore sizes also points towards a homogeneous oil distribution within the given pore size ranges, which is in line with reported Raman spectroscopy data. The observed reduction of gel and small capillary pore volume can be explained by the deployment of saponified layers on the pore wall surfaces, where they acted as a propagation and percolation barrier, and thus reduce the fluid and ion diffusion (for effects on durability see Section 3.5). Additionally, the significantly lower PSD evaluated by DVS analysis, directly indicates reduced water vapour diffusion (sorption and desorption) rates, which further induce the lower mass transport potential of the AAM_Moil composite.

MIP analyses (Fig. 6c) confirm the reduction of pore structure below 15 nm of R_p due to oil addition and the soap phase formation. The inflection point is at about 15-20 nm of the R_p (Fig. 6c, where the two curves intersect) which may be taken as significant pore size range upon

Table 3
MIP data of mortar composites.

	Apparent density (kg/m^3)	Pore volume (mm^3/g)	Total porosity (%)
AAM_M	2.09	203.8	27.81
AAM_Moil	1.92	199.8	28.89

which oil addition remarkably modifies pore structure. Meanwhile, oil addition generated a counter effect in the range of large capillary pores with a diameter above 100 nm and air voids above 5 μm (Fig. 6c) resulting in an overall similar total porosity and pore volume values (Table 3). This contrary effect within the larger fractions of the pore structure can be explained by alterations of the interfacial transition zone (ITZ) between the oil drops and the sand grains, where oil/water/activator emulsion accumulate around the sand grains and cause the formation of the larger, isolated pores, i.e. air voids. These singular air voids are most likely responsible for the observed lower strength values of AAM-Oil composites. This feature may have occurred due to inadequately optimized mixing procedure in respect to the oil distribution within the fresh mortar, allowing entrainment of bigger air bubbles, which were not homogenously mixed.

Light microscopy (Fig. 7a–b) and ESEM (Fig. 7c–d) images of the

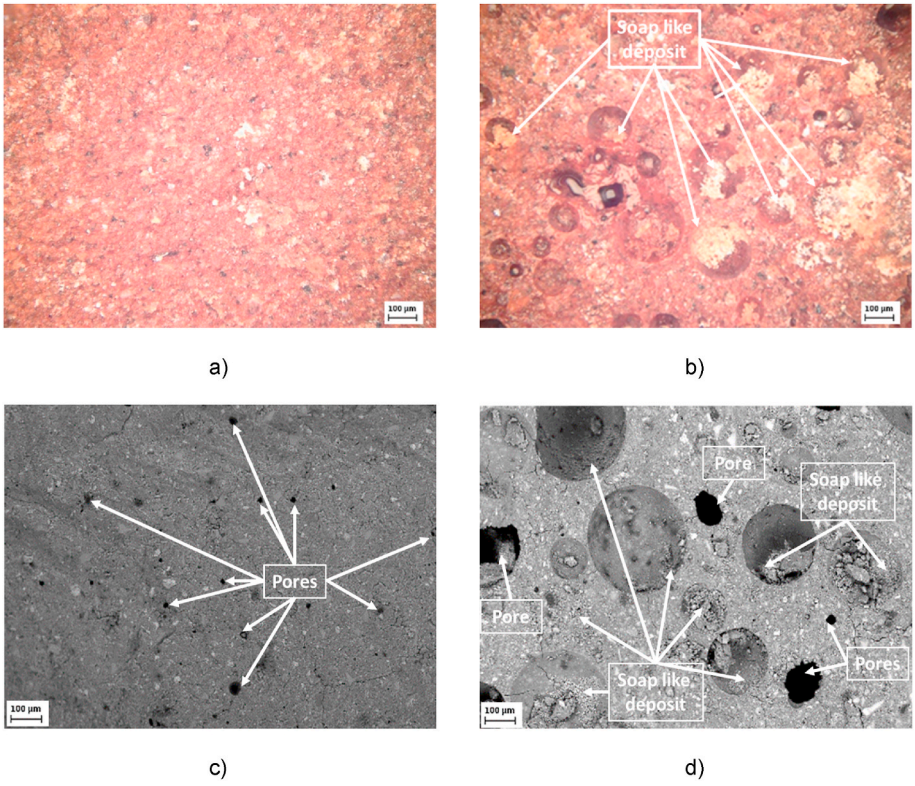

Fig. 7. Light microscope figures of a) AAM_P, b) AAM_Poil aged 28 days and c-d) ESEM figures of AAM_P and AAM_Poil.

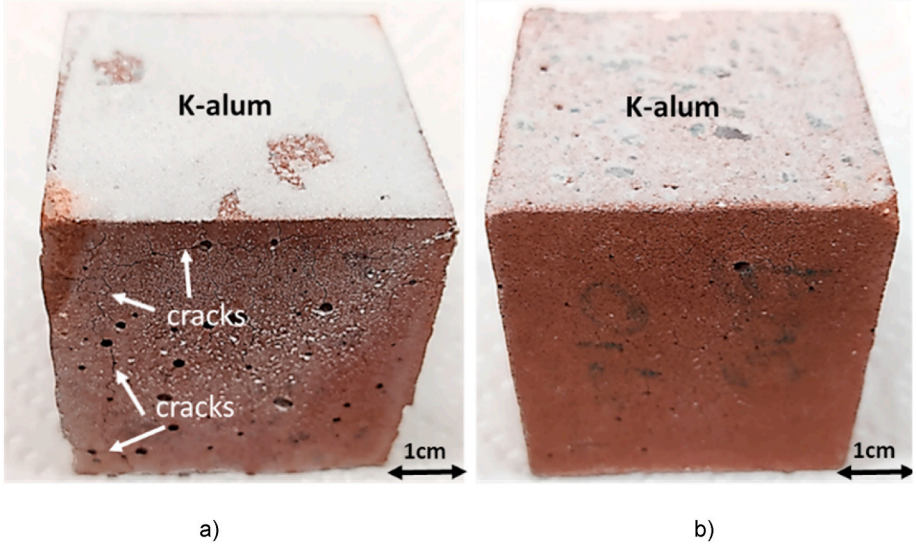

Fig. 8. Visual appearance of a) AAM_M and b) AAM_Moil specimens after the exposure to H_2SO_4 solution.

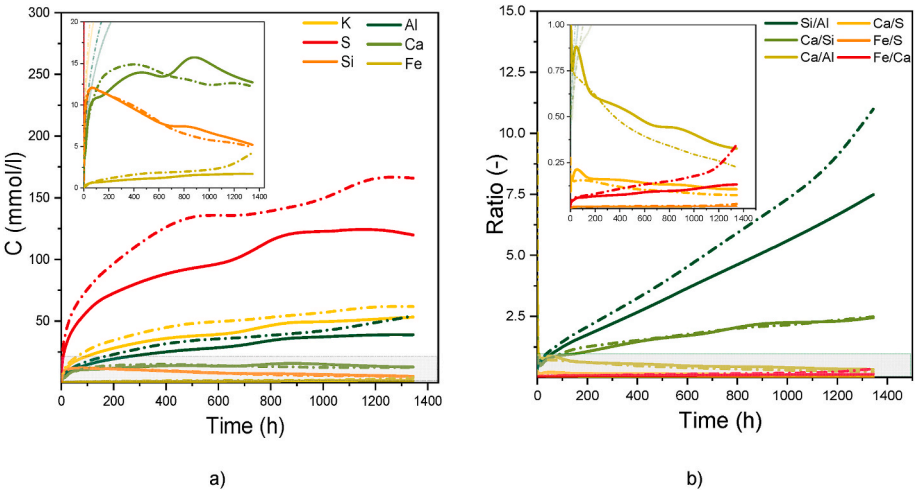

Fig. 9. Chemical evolution of the exposure solutions over time considering a) elemental concentrations and b) relevant elemental ratios (Si/Al, Al/K, Al/S, Ca/S) in case of AAM_M (chain lines) and AAM_Moil (solid lines). Please note shaded areas are enlarged in the upper left corners.

paste and mortar samples revealed the presence of large spherical air voids (diameter: 30–200 μm) in case of AAM_Poil samples. The observed air bubbles may be attributed to former oil droplets within the polymerized matrix. They do not possess an obvious interconnected structure, as the edges of air voids do not directly bridge neighbouring ones. Within the bubbles, whitish precipitates, most likely metal soap phases, appear. The existence of the spherical air voids is considered as the main reason for reduced compressive strength properties of AAM_oil system in comparison to AAM.

3.4. Effects of oil addition on the durability within acidic environments

In order to understand the impact of oil addition on the durability of AAMs in acidic environments, samples were exposed to sulfuric acid ($pH_{stat} = 2$) for 8 weeks at constant temperature (20 °C). Visual observations of the mortar specimens after exposure show several distinct differences between the AAM_M and the AAM_Moil composite (Fig. 8). While swelling, cracking or spalling cannot be noticed on the AAM_Moil composite, the AAM_M specimen shows an interconnected crack pattern. Additionally, significantly higher amounts of secondary phases, visible as whitish mineral precipitates on the AAM_M surface forms which may indicate an overall higher leaching rate for the AAM_M specimen vs. the sample with oil (Fig. 8).

Overall, a reduction of roughly 30% of acid dosage is observed for the AAM_Moil composite specimen. The evolution of dissolved ions and elemental ratios during exposure time of both types of mortar specimens is characterized by two main trends (Fig. 9). The first is marked by a rapid increase in concentration of dissolved species within the initial 24 h period representing a diffusion and leaching-controlled phase. It is followed by a period in which the concentration of dissolved species (Fig. 9a) is strongly reduced converging to a concentration plateau (or even in case of Si ions, is decreased), representing precipitation-controlled phase. A similar observation is also reported by Grengg et al. [31] where a detailed corrosion model was proposed for low Ca-AAMs.

In general, higher concentrations of dissolved ions are observed for the AAM_M compared to the AAM_Moil mortar sample, indicating different material degradation kinetics, including reduced material leaching and dissolution rates. The main reason for this behaviour is related to the strongly reduced acid diffusion rates due to the altered pore structure (Fig. 6). As a consequence, reduced precipitation of expansive secondary degradation products on the material surface and within the pore structure are observed. The DOC content of AAM_Moil did not exceed 0.23 g/dm^3 after 8 weeks of exposure accounting for total 3.9 wt% of the total organic carbon introduced by oil addition. How much of the dissolved organic carbon origins from soap phase and yet how much of glycerol and remaining oil, is a matter to be resolved in the following publication. This is a clear indication of the overall high stability of the formed soap phases in acidic environments. No DOC content was measured for the AAM_M specimens.

In order to further quantify the different material dissolution behaviour under acid exposure high resolution BSE and elemental maps were recorded (Fig. 10), while schematic description of the different deterioration zones is presented in Fig. 11. The deterioration within the AAM_M specimen follows the trend previously described by Grengg et al. [31]. In brief, the initial step of deterioration is marked by the leaching of K and S incorporation within the microstructure. The transition between the leached matrix (dissolution zone I, Fig. 11 left) and the strongly corroded microstructure is characterized by a sequence of elemental accumulations zones of Al, S and Ca (transition zone II, Fig. 11 left). This accumulation zone correspond to the formation of expansive secondary mineral phases, such as K-alum [$KAl(SO_4)_2{\cdot}12H_2O$], syngenite [$K_2Ca(SO_4)_2{\cdot}H_2O$], alunite [$KAl_3(SO_4)_2(OH)_6$], and anhydrite [$CaSO_4$], triggering micro- and macro-crack formation (Fig. 8 and Fig. 11 left). The strongly corroded, surface-near layers (dissolution zone I, Fig. 11 left) are characterized by a disrupted and strongly cracked microstructure, mainly composed of an amorphous Si-gel phase.

In contrast the AAM_Moil composite material shows a strongly divergent deterioration behaviour and a considerably lower depth of corrosion (dissolution zone I, Fig. 11 right). Therein, the transition between intact (unaffected zone III, Fig. 11 right) and corroded matrix (dissolution zone I, Fig. 11 right) is characterized by a strong reduction of Al, K and Ca and increasing Si concentrations. No elemental accumulation zones can be detected, except a thin transition layer (transition zone II, Fig. 11 right) where K and Ca leaching is followed by the framework dissolution zone, indicating strongly reduced precipitation of secondary corrosion products. Observed corrosion pattern argue for an overall high stability of the formed soap phases in acidic environments, aligning with the general stability of the polymeric framework. Accordingly, the deterioration process within AAM_Moil seems to have shifted from a diffusion- and crack-controlled process towards a framework dissolution process, progressing in layers, ultimately controlled by the intrinsic phase stability. As a result, significantly lower deterioration rates and approximately 70% lower sulphur ingress depths (i.e. 6 mm without oil vs. 2 mm with oil) are observed within the AAM_Moil composite material.

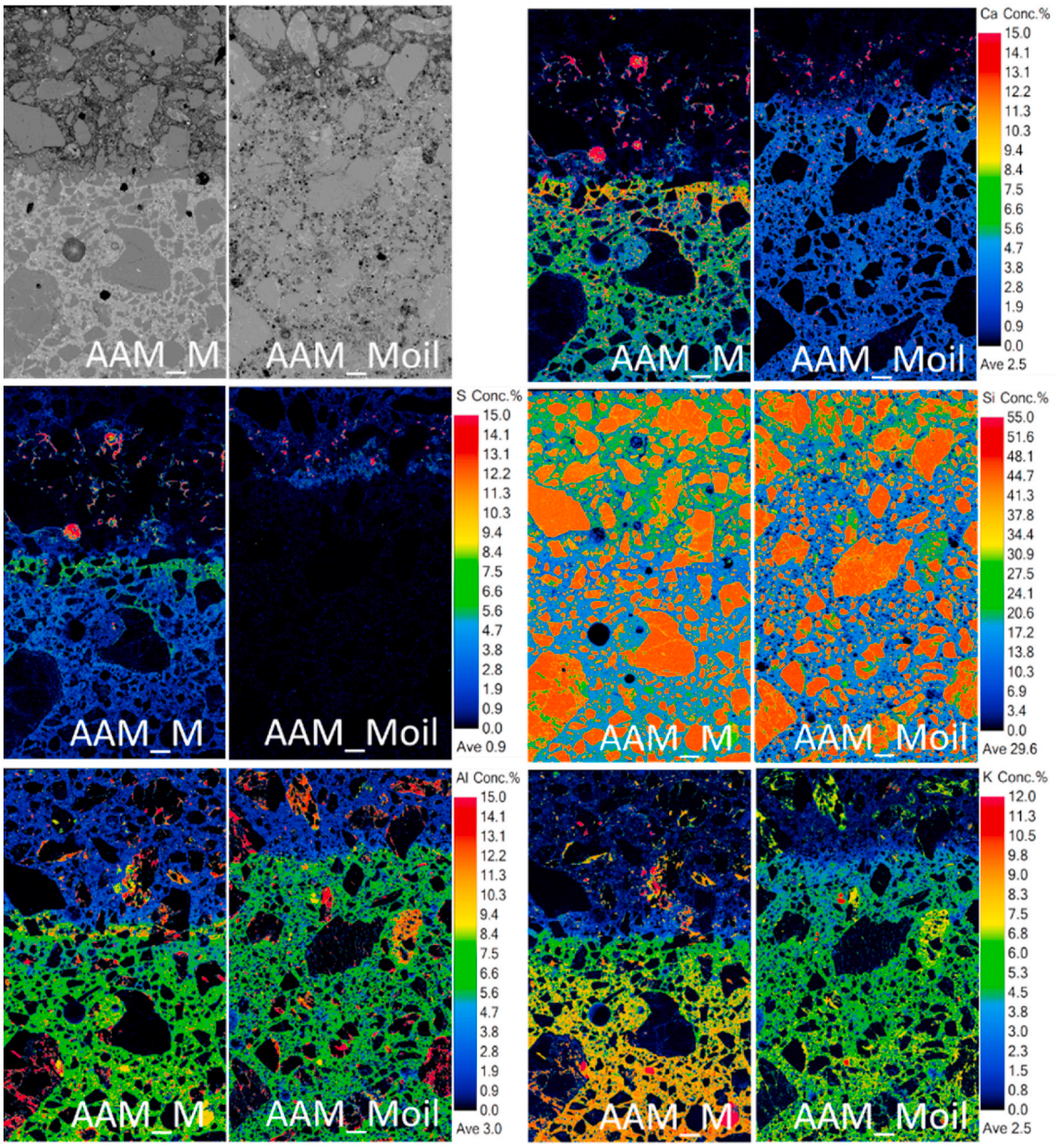

Fig. 10. High-resolution BSE and elemental distribution images of the AMM_M and AAM_Moil mortars after exposure to acid test.

4. Conclusions

The addition of sunflower oil to metakaolin-slag alkali activated binder had the following effects:

- Minimal impact on (geo)polymerization processes and reaction kinetics, but slight modification of the gel phase's polymerization/cross-linking degree.
- Considerable reduction in small capillary and gel pores, specific surface area (up to factor of 15) due to the formation of evenly distributed soap phases.
- Decreased compressive strength caused by the higher presence of large capillary pores (>0.1 μm) and entrained air voids (30–200 μm).
- Improved material stability in sulfuric acid environments, attributed to reduced acid diffusion kinetics and reduced precipitation of expansive (crack inducing) corrosion products.
- Potential to expand the range of AMMs applications by addressing weaknesses related to carbonation and chloride diffusion.

CRediT authorship contribution statement

Ognjen Rudić: Conceptualization, Methodology, Validation, Formal analysis, Investigation, Data curation, Writing – original draft, Writing – review & editing, Visualization. Florian Mittermayr: Conceptualization, Methodology, Validation, Writing – review & editing, Visualization, Funding acquisition, Project administration. Neven Ukrainczyk: Investigation, Writing – review & editing. Gregor Gluth: Formal analysis, Investigation, Writing – review & editing, Sebastian Simon: Formal analysis, Investigation. Bernhard Freytag: Review & editing, funding acquisition, Lead of Project. Seyrek Yunus: Review & editing, Joachim Juhart: Review & editing, funding acquisition, Project administration. Cyrill Grengg: Conceptualization, Methodology, Validation, Investigation, Writing – review & editing, Visualization, Funding acquisition.

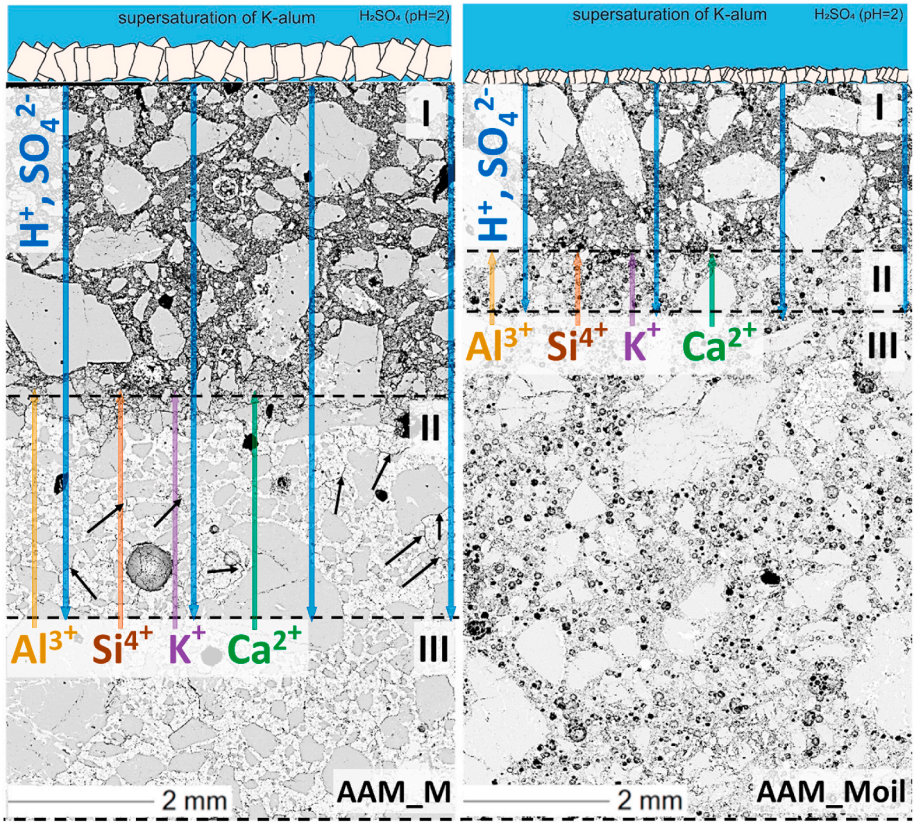

Fig. 11. Scheme of ongoing material dissolution behaviour under acid exposure with (I) dissolution zone, (II) transition zones/transition layer and (III) unaffected zone in case of AAM_M and AAM_Moil, respectively. Black arrows point to crack formation.

Declaration of competing interest

The authors declare that they have no known competing financial interests or personal relationships that could have appeared to influence the work reported in this paper.

Acknowledgement

The authors thank the Graz University of Technology (Austria) for scientific grant programs (FFG) for financial support realized through the funding under grant NR. 871279. The authors special thanks Dr. Andrew McIntosh, Post Graduate Researcher at Queen's University Belfast, for his valuable contribution regarding the raw materials data acquisition.

Appendix

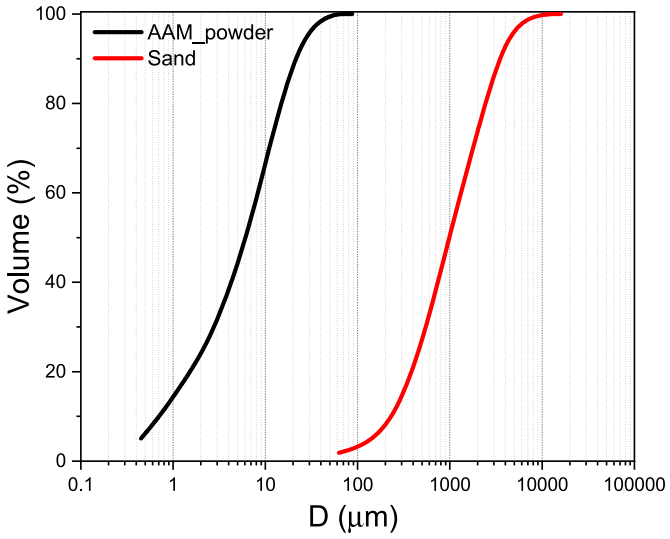

Fig. A1. Particle size distribution of AAM _powder (d_{50} = 6.11 μm; d_{90} = 21.44 μm) and sand aggregate

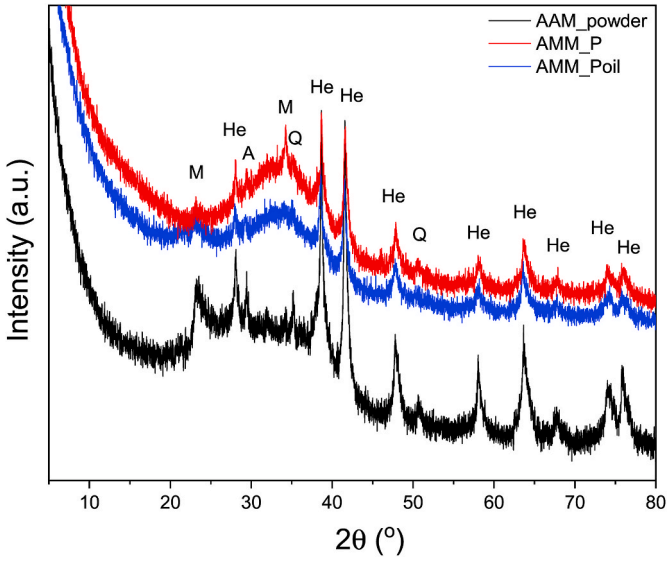

Fig. A2. XRD of AAM_powder and pastes. Mineral phases being found: He – hematite, M – meta-halloysite, A – anatas and Q – quartz. The diffractogram of the AAM_powder is included for comparison purposes

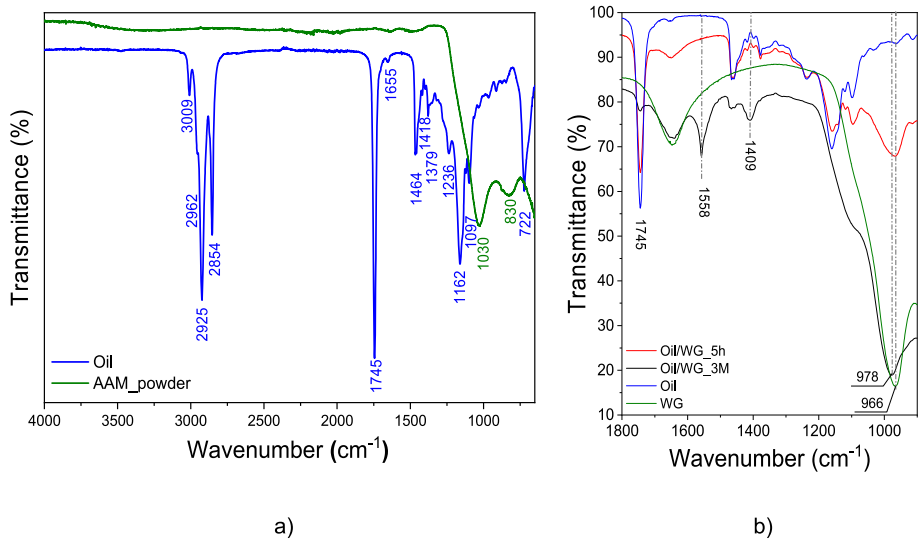

Fig. A3. FTIR spectra of a) AMM powder and oil; b) pure oil/WG mix (wavenumber range of 1800-900 cm^{-1})

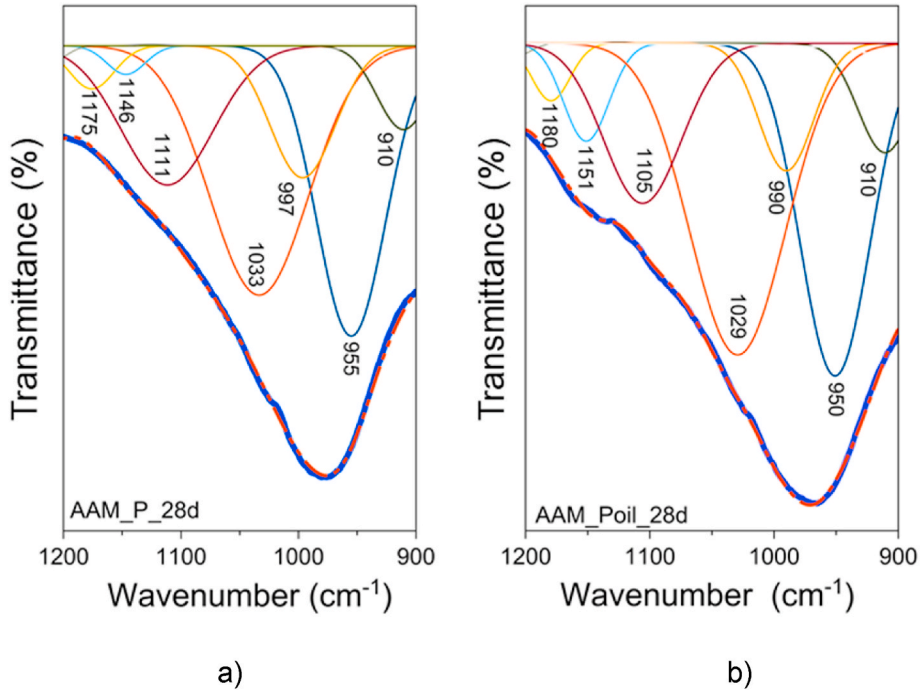

Fig. A4. ATR-FTIR spectra of deconvoluted FTIR spectra of a) AAM_P and b) AAM_Poil after 28 days of hardening within the wavenumber values range of 1200-900 cm^{-1}.

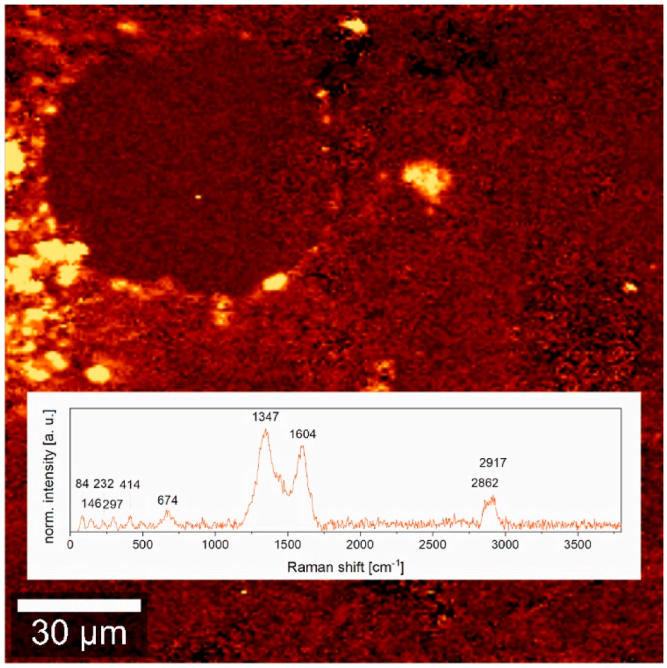

Fig. A5. Raman map of AAM_Poil, showing as bright regions the areas yielding a spectrum with a prominent peak in the range ~1575–1605 cm^{-1}, concentrated mainly around the air void in the top left corner. The inset shows a characteristic spectrum for the bright regions (characteristic peak at 1604 cm^{-1}).

Table A1
Functional groups and modes of vibration in the FTIR spectrum of AAM_powder, alkali activator and vegetable sunflower oil.

Wavenumber (cm^{-1})	Functional group assignment
AAM_powder	
1030	Si–O–Si(Al) molecular vibrations
830	Stretching vibration of Si–O–Si(Al) of different Al-coordination with a low degree of polymerization
750–650	bending vibrations of Si–O–Si(Al)
Sunflower oil	
3009	C–H stretching vibration of the *cis*-double bond (=CH)
2962; 2782	Symmetric and asymmetric stretching vibration shoulder of the aliphatic CH_3 group
2925; 2854	Symmetric and asymmetric stretching vibration of the aliphatic CH_2 group
1745	Ester carbonyl functional group of the triglycerides
1655	C═C stretching vibration of *cis*-olefins
1467–1458	Bending vibrations of the CH_2 and CH_3 aliphatic groups
1418	Rocking vibrations of CH bonds of *cis*-disubstituted olefins
1398	Bending in plane vibrations of CH *cis*-olefinic groups
1379	Bending vibrations of CH_2 groups
1236	Stretching vibration of the C O ester groups
1162	Stretching deformation of vibration of the C O ester groups
1097	Stretching vibration of the C–O ester group
722	Overlapping of the CH_2 rocking vibration and the out-of-plane vibration of *cis*-di-substituted olefins

References

[1] J.L. Provis, J.S.J. van Deventer, Alkali Activated Materials – State-Of-The-Art Report, RILEM TC 224-AAM, first ed., Springer Verlag, Berlin, 2014 https://doi.org/10.1007/978-94-007-7672-2.

[2] B. Singh, G. Ishwarya, M. Gupta, S.K. Bhattacharyya, Geopolymer concrete: a review of some recent developments, Construct. Build. Mater. 85 (2015) 78–90, https://doi.org/10.1016/j.conbuildmat.2015.03.03.

[3] K.L. Scrivener, V.M. John, E.M. Gartner, Eco-efficient cements: potential economically viable solutions for a low-CO_2 cement-based materials industry, Cement Concr. Res. 114 (2018) 2–26, https://doi.org/10.1016/j.cemconres.2018.03.015.

[4] J.L. Provis, S.A. Bernal, Geopolymers and related alkali-activated materials, Annu. Rev. Mater. Res. 44 (2014) 299–327, https://doi.org/10.1146/annurev-matsci-070813-113515.

[5] J.L. Provis, A. Palomo, C. Shi, Advances in understanding alkali-activated materials, Cement Concr. Res. 78A (2015) 110–125, https://doi.org/10.1016/j.cemconres.2015.04.013.

[6] J.L. Provis, Alkali-activated materials, Cement Concr. Res. 114 (2018) 40–48, https://doi.org/10.1016/j.cemconres.2017.02.009.

[7] T. Luukkonen, Z. Abdollahnejad, J. Yliniemi, P. Kinnunena, M. Illikainen, One-part alkali-activated materials: a review, Cement Concr. Res. 103 (2018) 21–34, https://doi.org/10.1016/j.cemconres.2017.10.001.

[8] S.A. Bernal, J.L. Provis, D.J. Green, Durability of alkali-activated materials: progress and perspectives, J. Am. Ceram. Soc. 97 (4) (2014) 997–1008, https://doi.org/10.1111/jace.12831.

[9] H. Ye, A. Radlińska, A review and comparative study of existing shrinkage prediction models for Portland and non-Portland cementitious materials, Adv. Mater. Sci. Eng. (2016) 1–13, https://doi.org/10.1155/2016/2418219.

[10] M. Mastali, P. Kinnunen, A. Dalvand, R. Mohammadi Firouz, M. Illikainen, Drying shrinkage in alkali-activated binders – a critical review, Construct. Build. Mater. 190 (2018) 533–550, https://doi.org/10.1016/j.conbuildmat.2018.09.125.

[11] B. Zhang, H. Zhu, P. Feng, P. Zhang, A review on shrinkage-reducing methods and mechanisms of alkali-activated/geopolymer systems: effects of chemical additives, J. Build. Eng. 49 (2022), 104056, https://doi.org/10.1016/j.jobe.2022.104056.

[12] P.H.R. Borges, B. Nemkumar, A.A. Himad, L. Wander, E. Vasconcelos, E.H. M. Nunes, Performance of blended metakaolin/blast furnace slag alkali-activated mortars, Cem. Concr. Compos. 71 (2016) 42–52, https://doi.org/10.1016/j.cemconcomp.2016.04.008.
[13] Y. Liu, Z. Yu, C. Lv, F. Meng, Y. Yang, Preparation of waste cooking oil emulsion as shrinkage reducing admixture and its potential use in high performance concrete: effect on shrinkage and mechanical properties, J. Build. Eng. 32 (2020), 101488, https://doi.org/10.1016/j.jobe.2020.101488.
[14] R.R. Nayaka, U.J. Alengaram, M.Z. Jumaat, S. Yusoff, R. Ganasan, Performance evaluation of masonry grout containing high volume of palm oil industry by-products, J. Clean. Prod. 220 (2019) 1202–1214, https://doi.org/10.1016/j.jclepro.2019.02.134.
[15] C. Wang, L. Xue, W. Xie, Z. You, X. Yang, Laboratory investigation on chemical and rheological properties of bio-asphalt binders incorporating waste cooking oil, Construct. Build. Mater. 167 (2018) 348–358, https://doi.org/10.1016/j.conbuildmat.2018.02.038.
[16] A. Svintsov, Y. Nikolenko, R. Fediuk, Aggressive effect of vegetable oils and organic fatty acids on cement-sand mortar and concrete, Construct. Build. Mater. 329 (2022), 127037, https://doi.org/10.1016/j.conbuildmat.2022.127037.
[17] N. Nestle, C. Zimmermann, M. Dakkouri, R. Niessner, Action and distribution of organic solvent contaminations in hydrating cement: time-resolved insights into solidification of organic waste, Environ. Sci. Technol. 35 (2001) 4953–4956, https://doi.org/10.1021/es015528y.
[18] S. Paria, P.K. Yuet, Solidification-stabilization of organic and inorganic contaminants using Portland cement: a literature review, Environ. Rev. 14 (2006) 217–255, https://doi.org/10.1139/a06-004.
[19] R. Abousnina, A. Manalo, W. Ferdous, W. Lokuge, B. Benabed, K. Saif Al-Jabri, Characteristics, strength development and microstructure of cement mortar containing oil-contaminated sand, Construct. Build. Mater. 252 (2020), 119155, https://doi.org/10.1139/a06-004.
[20] V. Cantarel, F. Nouaille, A. Rooses, D. Lambertin, A. Poulesquen, F. Frizon, Solidification/stabilisation of liquid oil waste in metakaolin-based geopolymer, J. Nucl. Mater. 464 (2015) 16–19, https://doi.org/10.1016/j.jnucmat.2015.04.036.
[21] V. Cantarel, D. Lambertin, A. Poulesquen, F. Leroux, G. Renaudin, F. Frizon, Geopolymer assembly by emulsion templating: emulsion stability and hardening mechanisms, Ceram. Int. 44 (2018) 10558–10568, https://doi.org/10.1016/j.ceramint.2018.03.079.
[22] C. Bai, P. Colombo, Processing, properties and applications of highly porous geopolymers: a review, Ceram. Int. 44 (2018) 16103–16118, https://doi.org/10.1016/j.ceramint.2018.05.219.
[23] M.S. Cilla, M.D. de Mello Innocentini, M.R. Morelli, P. Colombo, Geopolymer foams obtained by the saponification/peroxide/gel casting combined route using different soap foam precursors, J. Am. Ceram. Soc. 100 (2017) 3440–3450, https://doi.org/10.1111/jace.14902.
[24] C. Bai, J. Zheng, G.A. Rizzi, P. Colombo, Low-temperature fabrication of SiC/geopolymer cellular composites, Compos. B Eng. 137 (2018) 23–30, https://doi.org/10.1016/j.compositesb.2017.11.013.
[25] D.L. Rossatto, M.S. Netto, S.L. Jahn, E.S. Mallmann, G.L. Dotto, E.L. Foletto, Highly efficient adsorption performance of a novel magnetic geopolymer/Fe_3O_4 composite towards removal of aqueous acid green 16 dye, J. Environ. Chem. Eng. 8 (2020), 103804, https://doi.org/10.1016/j.jece.2020.103804.
[26] X. Zhang, C. Bai, Y. Qiao, X. Wang, D. Jia, H. Li, P. Colombo, Porous geopolymer composites: a review, Compos. Appl. Sci. Manuf. 150 (2021), 106629, https://doi.org/10.1016/j.compositesa.2021.106629.
[27] C. Bai, T. Ni, Q. Wang, H. Li, P. Colombo, Porosity, mechanical and insulating properties of geopolymer foams using vegetable oil as the stabilizing agent, J. Eur. Ceram. Soc. 38 (2018) 799–805, https://doi.org/10.1016/j.jeurceramsoc.2017.09.021.
[28] B. Planel, C.A. Davy, P.M. Adler, G. Hauss, M. Bertin, V. Cantarel, D. Lambertin, Water permeability of geopolymers emulsified with oil, Cement Concr. Res. 135 (2020), 106108, https://doi.org/10.1016/j.cemconres.2020.106108.
[29] C. Reeb, C. Pierlot, C. Davy, D. Lambertin, Incorporation of organic liquids into geopolymer materials - a review of processing, properties and applications, Ceram. Int. 47 (2021) 7369–7385, https://doi.org/10.1016/j.ceramint.2020.11.239.
[30] J. Huang, J. Yan, K. Liu, B. Wei, C. Zou, Influence of cooking oil on the mitigation of autogenous shrinkage of alkali-activated slag concrete, Materials 13 (2020) 4907, https://doi.org/10.3390/ma13214907.
[31] C. Grengg, G.J.G. Gluth, F. Mittermayr, N. Ukrainczyk, M. Bertmer, A. Guilherme Buzanich, M. Radtke, A. Leis, M. Dietzel, Deterioration mechanism of alkali-activated materials in sulfuric acid and the influence of Cu: a micro-to-nano structural, elemental and stable isotopic multi-proxy study, Cement Concr. Res. 142 (2021), 106373, https://doi.org/10.1016/j.cemconres.2021.106373.
[32] J. Juhart, C. Gößler, C. Grengg, F. Mittermayr, O. Rudic, A. McIntosh, B. Freytag, Material characterization of geopolymer mortar for its beneficial use in composite construction, RILEM Tech. Lett. 5 (2021) 174–185, https://doi.org/10.21809/rilemtechlett.2020.125.
[33] J. Kwasny, M.N. Soutsos, J.A. Mcintosh, D.J. Cleland, banahCEM - comparison of properties of a laterite-based geopolymer with conventional concrete, in: Proceedings of 9th International Concrete Conference 2016, 2016, pp. 383–394. Environment, Efficiency and Economic Challenges for Concrete.
[34] G. Brindley, K. Robinson, D. Macewan, The clay minerals halloysite and meta-halloysite, Nature 157 (1946) 225–226, https://doi.org/10.1038/157225b0.
[35] C.R. Kaze, P. Venyite, A. Nana, D.N. Juvenal, K. Tchakoute, H. Rahier, E. Kamseu, U.C. Melo, C. Leonelli, Meta-halloysite to improve compactness in iron-rich laterite-based alkali activated materials, Mater. Chem. Phys. (2019), 122268, https://doi.org/10.1016/j.matchemphys.2019.122268.
[36] L. Chen, Z. Wang, Y. Wang, J. Feng, Preparation and properties of alkali activated metakaolin-based geopolymer, Mater 9 (2016) 767, https://doi.org/10.3390/ma9090767.
[37] H. Rahier, B. Wullaert, B. Van Mele, Influence of the degree of dehydroxylation of kaolinite on the properties of aluminosilicate glasses, J. Therm. Anal. Calorim. 62 (2000) 417–427, https://doi.org/10.1023/A:1010138130395.
[38] N. Vlachos, Y. Skopelitis, M. Psaroudaki, V. Konstantinidou, A. Chatzilazarou, E. Tegou, Applications of Fourier transform-infrared spectroscopy to edible oils, Anal. Chim. Acta (2006) 573–574, https://doi.org/10.1016/j.aca.2006.05.034, 459–465.
[39] A. Rohman, Y.B. Che Man, Quantification and classification of corn and sunflower oils as adulterants in olive oil using chemometrics and FTIR spectra, Sci. World J. (2012), https://doi.org/10.1100/2012/250795.
[40] EN 196-1, Methods of Testing Cement - Part 1: Determination of Strength, 2016.
[41] EN 413-2, Masonry Cement - Part 2: Test Methods, 2016.
[42] A. Dakhane, S.B. Madavarapu, R. Marzke, N. Neithalath, Time, temperature, and cationic dependence of alkali activation of slag: insights from Fourier transform infrared spectroscopy and spectral deconvolution, Appl. Spectrosc. 71 (8) (2017) 1795–1807, https://doi.org/10.1177/0003702817704588.
[43] J. Zhang, C. Shi, Z. Zhang, Effect of Na_2O concentration and water/binder ratio on carbonation of alkali-activated slag/fly ash cements, Construct. Build. Mater. 269 (2021), 121258, https://doi.org/10.1016/j.conbuildmat.2020.121258.
[44] E.W. Washburn, The dynamics of capillary flow, Phys. Rev. 17 (1921) 73–283, https://doi.org/10.1103/PhysRev.17.273.
[45] S. Diamond, Mercury porosimetry: an inappropriate method for the measurement of pore size distributions in cement-based materials, Cement Concr. Res. 30 (2000) 1517–1525, https://doi.org/10.1016/S0008-8846(00)00370-7.
[46] N. Alderete, Y. Villagrán, A. Mignon, D. Snoeck, N. De Belie, Pore structure description of mortars containing ground granulated blast-furnace slag by mercury intrusion porosimetry and dynamic vapour sorption, Construct. Build. Mater. 145 (2017) 157–165, https://doi.org/10.1016/j.conbuildmat.2017.03.245.
[47] D. Snoeck, L.F. Velasco, A. Mignon, S. Van Vlierberghe, P. Dubruel, P. Lodewyckx, N. De Belie, The influence of different drying techniques on the water sorption properties of cement-based materials, Cement Concr. Res. 64 (2014) 54–62, https://doi.org/10.1016/j.cemconres.2014.06.009.
[48] V. Baroghel-Bouny, Water vapour sorption experiments on hardened cementitious materials: Part I: essential tool for analysis of hygral behaviour and its relation to pore structure, Cement Concr. Res. 37 (2007) 414–437, https://doi.org/10.1016/j.cemconres.2006.11.019.
[49] R. Snellings, J. Chwast, Ö. Cizer, N. De Belie, Y. Dhandapani, P. Durdzinski, J. Elsen, J. Haufe, D. Hooton, C. Patapy, M. Santhanam, K. Scrivener, D. Snoeck, L. Steger, S. Tongbo, A. Vollpracht, F. Winnefeld, B. Lothenbach, Report of TC 238-SCM: hydration stoppage methods for phase assemblage studies of blended cements - results of a round robin test, Mater. Struct. 51 (2018) 1–12, https://doi.org/10.1617/s11527-018-1237-5.
[50] E.P. Barrett, L.G. Joyner, P.P. Halenda, The determination of pore volume and area distributions in porous substances. I. Computations from nitrogen isotherms, J. Am. Chem. Soc. 73 (1951) 373–380, https://doi.org/10.1021/ja01145a126.
[51] S. Brunauer, P.H. Emmett, E. Teller, Adsorption of gases in multimolecular layers, J. Am. Chem. Soc. 60 (1938) 309–319, https://doi.org/10.1021/ja01269a023.
[52] J. Zhu, R. Zhang, Y. Zhang, F. He, The fractal characteristics of pore size distribution in cement-based materials and its effect on gas permeability, Sci. Rep. 9 (2019) 1–12, https://doi.org/10.1038/s41598-019-53828-5.
[53] Z. Zhang, H. Wang, J.L. Provis, F. Bullen, A. Reid, Y. Zhu, Quantitative kinetic and structural analysis of geopolymers. Part 1. The activation of metakaolin with sodium hydroxide, Thermochim. Acta 539 (2012) 23–33, https://doi.org/10.1016/j.tca.2012.03.021.
[54] Y. Ling, K. Wang, X. Wang, S. Hua, Effects of mix design parameters on heat of geopolymerization, set time, and compressive strength of high calcium fly ash geopolymer, Construct. Build. Mater. 228 (2019), 116763, https://doi.org/10.1016/j.conbuildmat.2019.116763.
[55] S.A. Bernal, J.L. Provis, V. Rose, R.M. de Gutierrez, Evolution of binder structure in sodium silicate-activated slag–metakaolin blends, Cem. Concr. Compos. 33 (2011) 46–54, https://doi.org/10.1016/j.cemconcomp.2010.09.004.
[56] Z. Zhang, J.L. Provis, H. Wang, F. Bullen, A. Reid, Quantitative kinetic and structural analysis of geopolymers. Part 2. Thermodynamics of sodium silicate activation of metakaolin, Thermochim. Acta 565 (2013) 163–171, https://doi.org/10.1016/j.tca.2013.01.040.
[57] J.L. Provis, J.S.J. van Deventer, Geopolymerisation kinetics. 2. Reaction kinetic modelling, Chem. Eng. Sci. 62 (2007) 2318–2329, https://doi.org/10.1016/j.ces.2007.01.028.
[58] S.K. Nath, S. Mukherjee, S. Maitra, S. Kumar, Kinetics study of geopolymerization of fly ash using isothermal conduction calorimetry, J. Therm. Anal. Calorim. 127 (2017) 1953–1961, https://doi.org/10.1007/s10973-016-5823-x.
[59] M. De Campos, C. Reeb, C.A. Davy, J. Hosdez, D. Lambertin, Solidification/stabilization (S/S) of high viscosity organics in geopolymers, J. Nucl. Mater. 571 (2022), 153979, https://doi.org/10.1016/j.jnucmat.2022.153979.
[60] R. Silverstein, F.X. Webster, D.J. Kiemle, Spectrometric Identification of Organic Compounds, sixth ed., John Wiley & Sons, Hoboken, 2006.
[61] G. Poulenat, S. Sentenac, Z. Mouloungui, Fourier-transform infrared spectra of fatty acid salts-Kinetics of high-oleic sunflower oil saponification, J. Surfactants Deterg. 6 (2003) 305–310, https://doi.org/10.1007/s11743-003-0274-1.

[62] M.E.S. Mirghani, Y.B.C. Man, S. Jinap, B.S. Baharin, J. Bakar, FTIR spectroscopic determination of soap in refined vegetable oils, J. Am. Oil Chem. Soc. 79 (2002) 111–116, https://doi.org/10.1007/s11746-002-0443-4.
[63] A. Rohman, Y.B.C. Man, Determination of sodium fatty acid in soap formulation using Fourier Transform Infrared (FTIR) spectroscopy and multivariate calibrations, J. Surfactants Deterg. 14 (2011) 9–14, https://doi.org/10.1007/s11743-010-1195-6.
[64] L. Robinet, M.C. Corbeil, The characterization of metal soaps, Stud. Conserv. 48 (2002) 23–40, https://doi.org/10.1179/sic.2003.48.1.23.
[65] M. Criado, A. Fernandez-Jimenez, A. Palomo, Alkali activation of fly ash: effect of SiO_2/Na_2O ratio: part I: FTIR study, Microporous Mesoporous Mater. 106 (2007) 180–191, https://doi.org/10.1016/j.micromeso.2007.02.055.
[66] I. Garcia-Lodeiro, A. Palomo, A. Fernandez-Jimenez, D.E. Macphee, Compatibility studies between N-A-S-H and C-A-S-H gels. Study in the ternary diagram Na_2O–CaO–Al_2O_3–SiO_2–H_2O, Cement Concr. Res. 41 (2011) 923–931, https://doi.org/10.1016/j.cemconres.2011.05.006.
[67] P. Yu, R.J. Kirkpatrick, B. Poe, P.F. McMillan, X. Cong, Structure of calcium silicate hydrate (C-S-H): near-, mid-, and far-infrared spectroscopy, J. Am. Ceram. Soc. 82 (1999) 742–748, https://doi.org/10.1111/j.1151-2916.1999.tb01826.x.
[68] N. Clayden, S. Esposito, A. Aronne, P. Pernice, Solid state ^{27}Al NMR and FTIR study of lanthanum aluminosilicate glasses, J. Non-Cryst. Solids 258 (1999) 11–19, https://doi.org/10.1016/S0022-3093(99)00555-4.
[69] M. Król, P. Rożek, D. Chlebda, W. Mozgawa, Influence of alkali metal cations/type of activator on the structure of alkali-activated fly ash–ATR-FTIR studies, Spectrochim, Acta A Mol. Biomol. Spectrosc. 198 (2018) 33–37, https://doi.org/10.1016/j.saa.2018.02.067.
[70] S. Zhang, Z. Li, B. Ghiassi, S. Yin, G. Ye, Fracture properties and microstructure formation of hardened alkali-activated slag/fly ash paste, Cement Concr. Res. 144 (2021), https://doi.org/10.1016/j.cemconres.2021.106447.
[71] B. Walkley, R. San Nicolas, M. Sani, G.J. Rees, J.V. Hanna, J.S.J. van Deventer, J. L. Provis, Phase evolution of C-(N)-A-S-H/N-A-S-H gel blends investigated via alkali-activation of synthetic calcium aluminosilicate precursors, Cement Concr. Res. 89 (2016) 120–135, https://doi.org/10.1016/j.cemconres.2016.08.010.
[72] K. Juengsuwattananon, F. Winnefeld, P. Chindaprasirt, K. Pimraksa, Correlation between initial SiO_2/Al_2O_3, Na_2O/Al_2O_3, Na_2O/SiO_2 and H_2O/Na_2O ratios on phase and microstructure of reaction products of metakaolin-rice husk ash geopolymer, Construct. Build. Mater. 226 (2019) 406–417, https://doi.org/10.1016/j.conbuildmat.2019.07.146.
[73] C.K. Yip, G.C. Lukey, J.S.J. Van Deventer, The coexistence of geopolymeric gel and calcium silicate hydrate at the early stage of alkaline activation, Cement Concr. Res. 35 (2005) 1688–1697, https://doi.org/10.1016/j.cemconres.2004.10.042.
[74] S. Puligilla, X. Chen, P. Mondal, Understanding the role of silicate concentration on the early-age reaction kinetics of a calcium containing geopolymeric binder, Construct. Build. Mater. 191 (2018) 206–215, https://doi.org/10.1016/j.conbuildmat.2018.09.184.
[75] I. Ismail, S.A. Bernal, J.L. Provis, R. San Nicolas, S. Hamdan, J.S.J. van Deventer, Modification of phase evolution in alkali-activated blast furnace slag by the incorporation of fly ash, Cem. Concr. Compos. 45 (2014) 125–135, https://doi.org/10.1016/j.cemconcomp.2013.09.006.
[76] R.J. Myers, E. L'Hopital, J.L. Provis, B. Lothenbach, Composition-solubility-structure relationships in calcium (alkali) aluminosilicate hydrate (C-(N,K-)A-S-H), Dalton Trans. 44 (2015) 13530–13544, https://doi.org/10.1039/C5DT01124H.
[77] B. Liu, K. Zhuang, D. Li, Y. Fang, G. Pan, Understanding the early reaction and structural evolution of alkali activated slag optimized using K-A-S-H nanoparticles with varying K_2O/SiO_2 ratios, Comp. B: Eng. 200 (2020), 108311, https://doi.org/10.1016/j.compositesb.2020.108311.
[78] The RRUFF Project. https://rruff.info/. (Accessed 20 January 2022).
[79] B. Lafuente, R.T. Downs, H. Yang, N. Stone, The power of databases: the RRUFF project, in: T. Armbruster, R.M. Danisi (Eds.), Highlights in Mineralogical Crystallography, De Gruyter, Berlin, 2015, pp. 1–30, https://doi.org/10.1515/9783110417104-003.
[80] R.L. Frost, H.F. Shurvell, Raman microprobe spectroscopy of halloysite, Clay Clay Miner. 45 (1997) 68–72, https://doi.org/10.1346/CCMN.1997.0450107.
[81] J.T. Kloprogge, R.L. Frost, Raman microprobe spectroscopy of hydrated halloysite from a neogene cryptokarst from Southern Belgium, J. Raman Spectrosc. 30 (1999) 1079–1085, https://doi.org/10.1002/(SICI)1097-4555(199912)30:12<1079::AID-JRS488>3.0.CO;2-G.
[82] R.L. Frost, The structure of the kaolinite minerals — a FT-Raman study, Clay Miner. 32 (1997) 65–77, https://doi.org/10.1180/claymin.1997.032.1.08.
[83] A. Flack, Discrimination of Cooking Oils Using Raman Spectroscopy, Application Note AN_R03, Edinburgh Instruments, 2019. https://www.edinst.com/discrimination-of-cooking-oils-using-raman-spectroscopy/.
[84] H.Y. Lam, P.K. Roy, S. Chattopadhyay, Thermal degradation in edible oils by surface enhanced Raman spectroscopy calibrated with iodine values, Vib. Spectrosc. 106 (2020), 103018, https://doi.org/10.1016/j.vibspec.2019.103018.
[85] K. Czamara, K. Majzner, M.Z. Pacia, K. Kochan, A. Kaczor, M. Baranska, Raman spectroscopy of lipids: a review, J. Raman Spectrosc. 46 (2015) 4–20, https://doi.org/10.1002/jrs.4607.
[86] X. Ke, S.A. Bernal, T. Sato, J.L. Provis, Alkali aluminosilicate geopolymers as binders to encapsulate strontium-selective titanate ion-exchangers, Dalton Trans. 48 (2019) 12116–12126, https://doi.org/10.1039/c9dt02108f.
[87] Y. Zuo, M. Nedeljkovic, G. Ye, Coupled thermodynamic modelling and experimental study of sodium hydroxide activated slag, Construct. Build. Mater. 188 (2018) 262–279, https://doi.org/10.1016/j.conbuildmat.2018.08.087.
[88] S.A. Bernal, E.D. Rodríguez, R. Mejía de Gutierrez, M. Gordillo, J.L. Provis, Mechanical and thermal characterisation of geopolymers based on silicate-activated metakaolin/slag blends, J. Mater. Sci. 46 (2011) 5477–5486, https://doi.org/10.1007/s10853-011-5490-z.
[89] S.A. Bernal, R. Mejia de Gutiérrez, J.L. Provis, V. Rose, Effect of silicate modulus and metakaolin incorporation on the carbonation of alkali silicate-activated slags, Cement Concr. Res. 40 (2010) 898–907, https://doi.org/10.1016/j.cemconres.2010.02.003.
[90] X. Zhou, X. Li, B. Zhao, X. Chen, Q. Zhang, Discriminant analysis of vegetable oils by thermogravimetric-gas chromatography/mass spectrometry combined with data fusion and chemometrics without sample pretreatment, LWT 161 (2022), 113403, https://doi.org/10.1016/j.lwt.2022.113403.